CHAPTER 4

Topological Insulating Phase in Some Low Dimensional Materials

In this chapter we discuss three methods such as, dimensional engineering, application of stress/strain and, partial functionalization, by which non-trivial topological insulating nature can be realised in two dimensional materials LiMgAs, AuI, Tellurene and Selenene. We discuss these non-trivial character in terms of qualitative and quantitative analysis (similar to that in chapter 3) wherein we present, non-trivial band and orbital inversions, unconventinal Berry and spin-Berry curvature, quantum conductivity, $\mathbb{Z}_2$ invariant (ν), angle resolved photoemission spectroscopy-like egde state spectra and slab band structures. Apart from this, we also discuss methods to practically realise such materials. These studies are presented with investigation of material stability in terms of phonon dispersion curves, AIMD etc.

4.1 Dimensionally Engineered Topological Insulator: LiMgAs

Over the past two decades, low dimensional topological materials such as, two dimensional topological insulators have sparked immense excitement in the field of condensed matter physics. This is because of the non-trivial characteristics such as, insulating bulk and helical edge conducting states.[1–5] These states are robust against material impurities and back-scattering which ensures dissipationless transport of electrons in perpetual helical paths along the edges. Eversince the prediction of topological insulators in low dimensional systems such as, graphene and HgTe/CdTe quantum wells, several materials have been predicted and experimentally realised to host the topological insulating nature.[6–12] Similar to the bulk materials where the spin-orbit interactions were enhanced by various mechanisms, in the low dimensional materials several techniques have been explored to realise similar effects. For example, in order to enhance the spin-orbit interactions in low dimensional materials and to induce non-trivial topological properties in them via topological quantum phase transitions, techniques such as, (i) application of strain/pressure, (ii) doping, (iii) variation of layer thickness, (iv) van der Waals layered systems or stacking effect and, (v) application of electric field etc. have been proposed. Also, elemental monolayers such as, silicene, germanene and stanene are known to exhibit non-trivial topological insulating nature by the virtue of enhanced spin-orbit interactions which originate from the buckling in these monolayers.[8–12] However, buckling solely does not gaurantee that the system would be topologically non-trivial. For example, arsenene and antimonene exhibit buckled structure but, these monolayers are non-trivial only under the influence of tensile strain.[11,12] Although, these low dimensional materials exhibit non-trivial topologies, they are inefficient and tough to be realised at room temperatures since, the spin-orbit interactions induced global gap in the brillouin zone are smaller than the thermal perturbations at room temperature. This indicates that, there is a lot of scope to explore other potential materials which can have room temperature applications. This motivated us to explore low dimensional materials for non-trivial topological properties.

There are several methods by which we can design low dimensional materials such as, free standing structures, structures supported by substrates etc. Here, we began our investigations by dimensionally engineering low dimensional structures from bulk crystal surfaces. This was achieved by isolating and confining the material along a particular crystal direction. For example, we performed one dimensional confinement of [111] crystal plane cleaved from the bulk half-heusler compound LiMgAs. This dimensionally engineered system was investigated for non-trivial topological properties originating from the quantum confinement effects. We observed that, the low dimensional material designed by such method is superior as compared to their bulk parents. Therefore, we successfully address the issues which we came across in material design as discussed in previous chapters. For example, as proposed in previous chapter, we do observe non-trivial topologies in low dimensional phase as compared to the trivial topologies in the bulk parent. Also, since the surface-to-volume ratio is high, the pressure required to realised non-trivial topologies is quite low as compared to the bulk. Such method of material design is reliable since, it has been previously explored in NbN wherein, the [100] and [111] crystal planes were isolated by dimensional engineering from the rocksalt parent structure for photocatalytic and piezoelectric applications.[13] This method can also be thought of as an analogoue to the variation of thickness of the material wherein, by reducing the layers of a material, eventually a monolayer is achieved (as in the case of graphene which is a monolayer of graphite).

Structure and Lattice Dynamics

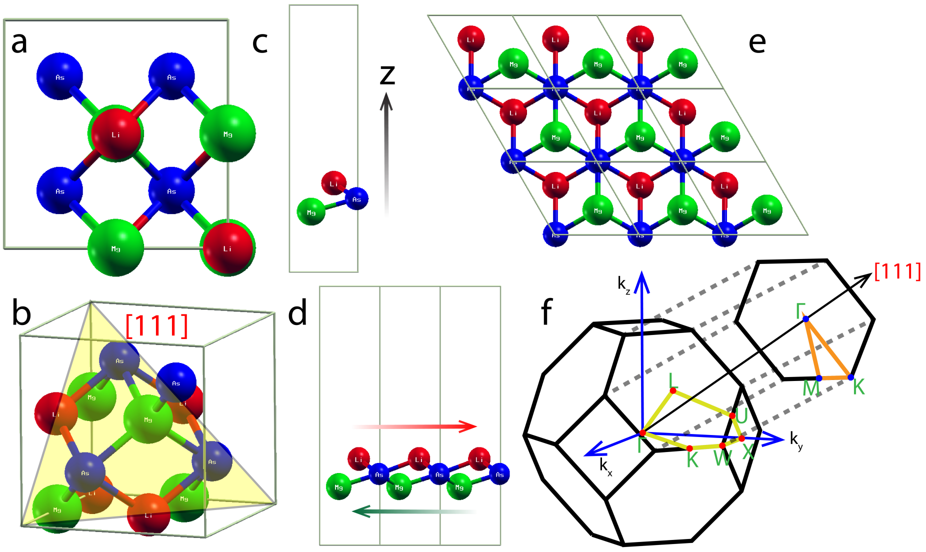

Figure 4.1: (a) Bulk structure of half-heusler LiMgAs and its [111] crystal plane (b). (c) One dimensional quantum confinement by introducing 15 Å vacuum in z-direction. (d, e) Side and top view of the low-dimensional supercell. (f) Irreducible first brillouin zones of the bulk and low-dimensional of LiMgAs.

We designed a low dimensional phase of LiMgAs by cleaving [111] crystal plane from the bulk face centered cubic structure and isolating it along the z-direction by introducing a vacuum (as presented in Fig. 4.1(a-c)). Under generalised gradient approximations, this structure exhibits a trigonal structure governed by the $P\bar{3}m1[164]$ space group (similar to 1T-MoS_2) with optimized lattice constant (a) of 4.28 Å (as evident from Fig. 4.1(c)). We can think of this structure as an atomic sandwich wherein, As atoms are stuffed between the top layer of Li and bottom layer of Mg as presented in Fig. 4.1(d,e). The thickness (layer height) of such atomic sandwich is 1.60 Å. Here, the interatomic distances of As-Mg and As-Li are 2.58 Å and 2.62 Å respectively. The quantum confinement along one dimension is

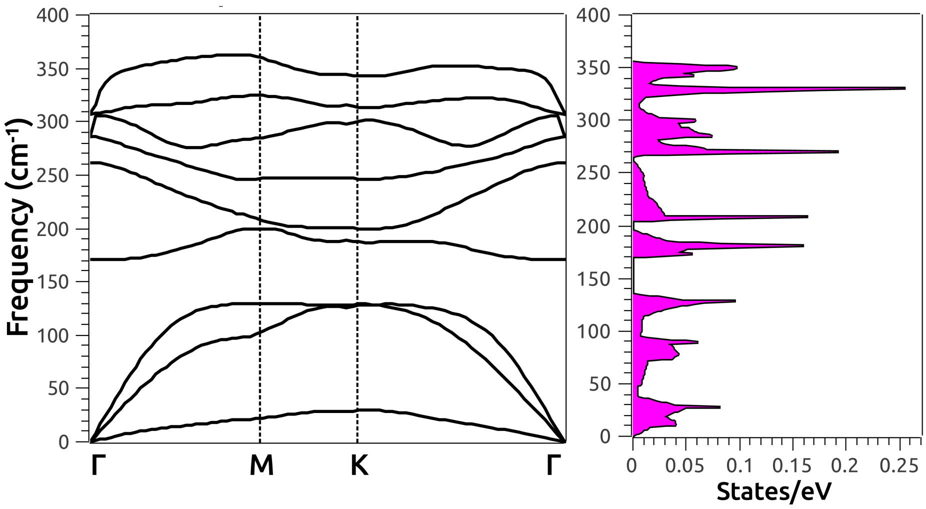

Figure 4.2: Phonon dispersion curves and density of states indicating dynamic stability of low dimensional LiMgAs.

achieved due to the vacuum of 15 (Å) along the z-direction which is also inntroduced to avoid interlayer interactions or interactions between the periodic images as show in Fig. 4.1(c).

Since this structure is being predicted for the first time, we investigated its dynamic stability (in terms of the phonon dispersion curves and phonon density of states) to comment on the experimental feasibility of such structure. From our computations of the phonon dispersion curves and the phonon density of states presented in Fig. 4.2, it is clear that, the absence of negative phonon frequencies throughout the brillouin zone indicate towards the dynamic stability of the proposed structure. The unit cell of the proposed structure hosts three atoms giving rise to nine phonon branches similar to the bulk parent. Contrary to the bulk phase wherein, the nine phonon branches were composed of three in plane acoustic branches (dominant at lower frequencies) and six optical branches (dominant at higher frequencies), the nine phonon branches in the low dimensional phase exhibits are composed of, three in plane acoustic branches, three out-of-plane acoustic (ZA) and optical (ZO) branches (due to the one dimensional quantum confinement owing to the 15 Å vacuum along z-direction) and, three optical branches.

Electronic Properties

The low dimensional phase of LiMgAs exhibits a semi-conducting nature with a direct band gap of 1.56 eV at the center of the brillouin zone (as evident from Fig. 4.3) as compared to the bulk which had a slightly smaller indirect band gap. This is due to the quantum confinement effects wherein, the electronic degrees of freedom are different as compared to the bulk. Throughout the brillouin zone the conduction band and valence band frontiers are non-degenerate. However, in the vicinity of Fermi, the valence band maxima along the high symmetry paths, L → Γ and W → X is degenerate while, along the paths X → U → L and Γ → K → W they are non-degenerate (as evident from Fig. 2.27). This feature is exactly similar to the bulk parent.

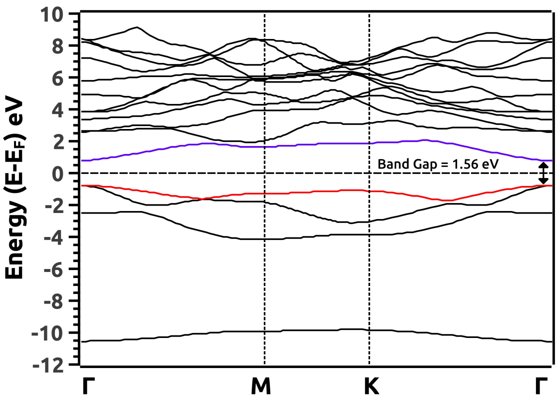

Figure 4.3: Electronic band structure of low dimensional LiMgAs.

On imposing isotropic compressive pressure on the low dimensional structure of LiMgAs we observed that, the band gap reduces; eventually forming a Dirac degeneracy (at 10% compressive pressures presented in Fig. 4.4) at the center of the brillouin zone (Γ) marking the critical point in the topological quantum phase transition. The Dirac degeneracy of the conduction and valence band frontiers; exhibit remarkable Fermion velocities.[14] The conduction band minima hosts Fermion velocities of the order of $v_f \sim 0.56$ ms^{-1} and ~ 1.31 ms^{-1} along the high symmetry path K → Γ and Γ → M respectively in the brillouin zone. Similarly, the valence band maxima hosts Fermion velocities of the order of, $v_f \sim 11.13$ ms^{-1} and ~ 7.64 ms^{-1} along high symmetry path K → Γ and Γ → M respectively in the brillouin zone. These Fermion velocities are comparable to that of graphene (in a particular momentum direction) and superior to other two dimensional materials. Owing to the extra electronic degrees of freedom due to quantum confinement, the low dimensional exhibits higher Fermion velocities as compared to the bulk parent. Beyond the critical point (which hosts Dirac degeneracies at the center of brillouin zone) in the topological quantum phase transition, the bulk electronic band structure hosts a global gap in the brillouin zone. Also, as evident from Fig. 4.4(right), the band degeneracy in the valence band maxima lifts off giving rise to Fermionic contributions in the vacant conduction band.

With further increase in the compressive pressure we observed topological quantum phase transition i.e., the Dirac degeneracy at Γ lifts off creating a gap which indicates the topological insulating nature. This critical pressure is quite small (2.96 GPa) as compared to

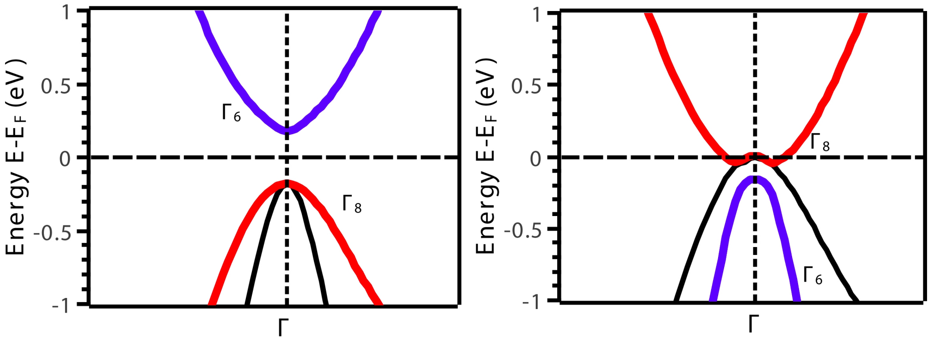

Figure 4.4: Electronic band structure of low dimensional LiMgAs at (left) 8% and (right) 10% pressure.

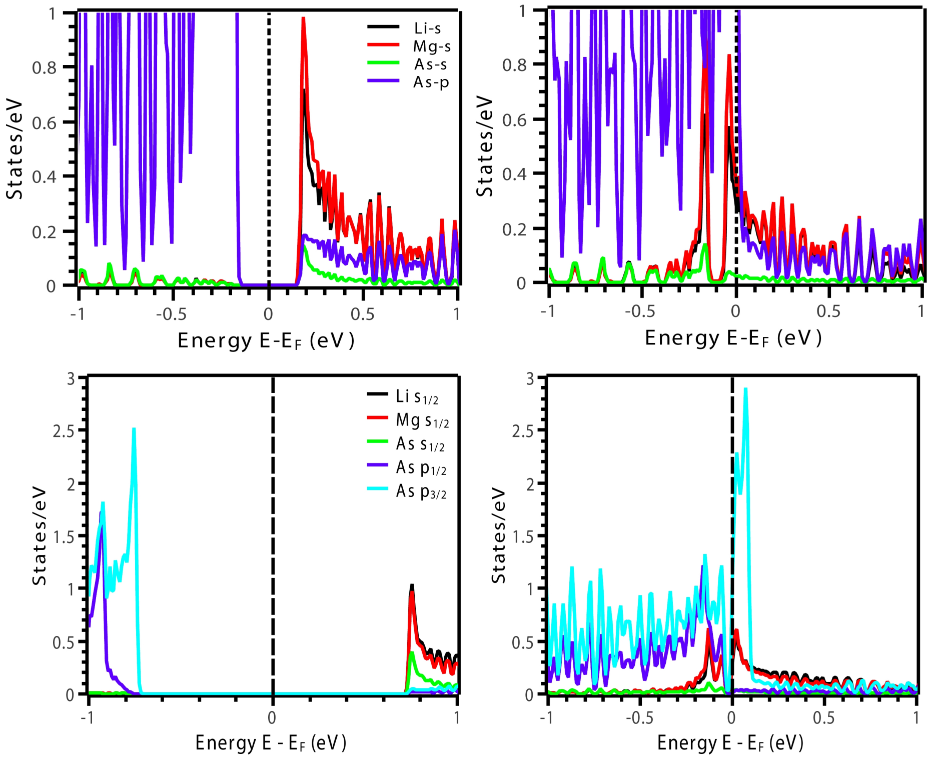

Figure 4.5: Orbital projected density of states without spin-orbit interactions (top) and with spin-orbit interactions (bottom) before (left) and at critical pressure (right) respectively, hosting exchanged orbital features around Fermi.

the bulk parent wherein the pressure was of the order of 8.18 GPa. The non-trivial topological quantum phase transition can be analysed in terms of the orbital projected density of states which indicates the exchange of orbital contributions across the Fermi level. From the orbital projected density of states presented in Fig. 4.5, we observe that, the orbital exchange is quite strong as compared to that in the bulk phase.

The proposed low dimensional LiMgAs exhibits orbital orders similar to that of the bulk parent i.e., the valence band is populated by the *p*-orbital and the conduction band is populated by the *s*-orbital. Under critical compressive pressure, the *s*-orbitals in conduction band penetrate the valence band and the *p*-orbital from valence band penetrates the conduction band. Such band orbital order is somewhat similar to that of HgTe.[15] This implies that, the *p*-orbital Fermions of As atom are the major contributors to the observed non-trivial topological insulating nature. In the proposed low dimensional LiMgAs, the band inversion strength is positive and strong i.e., $\Delta \sim 113.7$ meV as compared to the bulk parent favouring non-trivial phase of LiMgAs in the proposed low dimensional structure.[15,16] When, the spin-orbit interactions (which is quite pronounced in this phase due to buckling as compared to the bulk phase) are considered a global gap of ~ 55.0 meV is observed while the non-global gap is as high as 0.16 eV.[10] This is superior to graphene, silicene, arsenene etc.[6,11,17] Figure 4.6(left) and (right) represent; the band inverted dispersions with and without the spin-orbit interactions (under critical pressure), alongside the schematic inversion mechanism in terms of orbital contributions under 0% and 10% pressure respectively. The band dispersions due to spin-orbit interactions indicates that, the proposed low dimensional phase can have applications in spintronics at room temperature.[18,19]

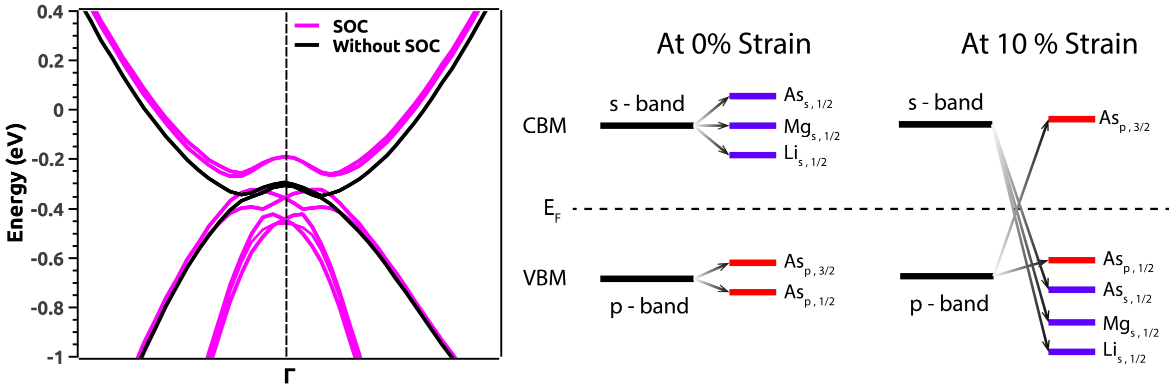

Figure 4.6: (left) Electronic band dispersions of low dimensional LiMgAs with and without spin-orbit interactions (under critical pressure). (right) Schematic representation of the orbital inversion mechanism due to pressure and spin-orbit interactions at 0% and 10% pressure.

Topological Properties

Following the qualitative description of non-trivial topological quantum phase transitions in the low dimensional phase of LiMgAs, we now discuss the quantitative descriptions in terms of the angle resolved photoemission spectroscopy-like spectra and $\mathbb{Z}_2$. Figure 4.7 represents the conducting edge states in the presence of the spin-orbit interaction induced bulk gap (under critical pressure). These non-trivial edge states are confirmed for their non-trivial character

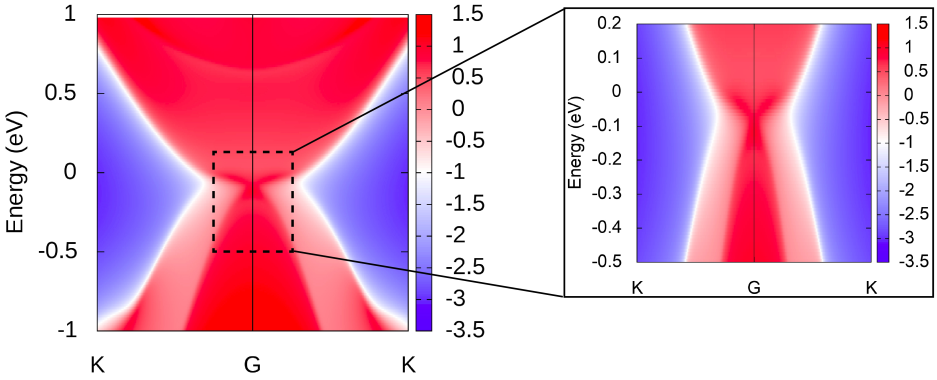

Figure 4.7: Angle resolved photoemission spectroscopy-like spectra indicating conducting edge states.

by computing the $\mathbb{Z}_2$ invariant (ν). We can compute the $\mathbb{Z}_2$ by using Fu and Kane method discussed in chapter 2 and/or by computing the wannier charge centers across the Fermi at time reversal invaraint planes. We find that, the $\mathbb{Z}_2$ is $\nu = 1$ confirming the non-trivial nature topological insulating nature of low dimensional LiMgAs as compared to the trivial bulk. This affirmatively confirms that, dimensional engineering method can be used to realise non-trivial topological materials from trivial bulk parents.

4.2 Functionalization; a Tool for Large-gap Topological Insulator

For room temperature applications in, spintronics, valleytronics, electronic and quantum computation, the persistance of conducting edge states (robust against weak deformations and external perturbations) are necessary. This is possible if the low dimensional material possesses large-gap due to spin-orbit interactions. If the gap is smaller than the thermal energy at room temperature then, irrespective of symmetry protection, the conducting edge states would annihilate. This indicates that, a large-gap low dimensional topological insulator is desired and needed for practical applications which would host, gapless spin-polarized helical edge states with non-magnetic insulating global gap in bulk, spin currents protected against backscattering and, quantized Hall conductance without magnetic field.

Although, graphene and other group IV and V elements have been previously explored for non-trivial topological insulating nature from theoretical perspective but, phenomena could be observed experimentally at ultra-low temperatures and ultra-high pressures in quantum wells of HgTe/CdTe and InAs/GaSb.[20–32] This has motivated numerous investigations based on *first-principles* and theorical modelling methods guiding the experimental efforts. Inspite of several methods proposed theoretically, one of the persistant problems is realising large-gap low dimensional topological insultors. As an alternative, this had been addressed by using functionalization techniques in monolayers of group IV, V; Xene's and MXene's etc. The governing phenomena is that of orbital filtering effect wherein, *pz*-orbitals in the monolayer are saturated by the functional molecule which enhances the spin-orbit interactions.[24,33–43] This technique has been found to be viable experimentally. For example, halogenation of Bi monolayers was observed to induce non-trivial topological insulating states. However, these states were sensitive to hybridizations with the substrates which made it less reliable. Apart from this, other problems such as, effects of environmental oxidation and eventual degradation of the edge state makes low dimensional topological insulators vulnerable; hindering their practical applications.[44]

Inspired by the investigation of group IV and V elemental monolayers for non-trivial topologies, efforts were made to explore similar features in group VI Xene's with honeycomb lattice structure for example, in tellurium and selenium based monolayers. It was speculated that, honeycomb lattice structure cannot be achieved with tellurium and selenium owing to their electronic configurations. Rather, these elemental monolayers have been observed to exhibit ring, chain, square and rectangular lattice structures.[31,42,47] Contrary to such studies, in an experimental effort, recently it was observed that, thickness-dependent transition from Au-Te surface alloy to honeycomb lattice of tellurium (i.e., 3×3 superstructures) can be achieved due to the fact that, Tellurium atoms self-organise themselves on Au[111] surface (under high temperatures and ultra-high vacuum) with 0.5 monolayer coverage.[48] This motivated us to ask the question, are there any other alternatives by which we can realise dynamically stable honeycomb lattice structure of tellurium and selenium? Also, if such alternative exists, leading to the monolayers tellurene and selenene then, can they host non-trivial topologies?

We addressed these questions by employing *first-principles* computation to investigate, (i) the stability of tellurene and selenene, (ii) the role of *functionalization* in the stability of such monolayers and (iii) the corresponding effects on the on-trivial topological properties. We found that, pristine elemental monolayers of tellurene and selenene are not dynamically stable, which is in agreement with previous studies.[49] However, on performing functionalization with oxygen and sulphur, the dynamic stability was achieved. We found that, upon functionalization, by the virtue of orbital filtering effects the proposed monolayers host large-gap topological insulating behaviour due to strong spin-orbit interactions. This implies that, the proposed monolayers can be experimentally viable for potential applications. We restrict our discussions to non-trivial topological properties observed in oxygen functionalised tellurene and sulphur functionalised selenene, since these materials host large-gap governed by spin-orbit interactions which are superior to several other materials.

Structure and Lattice Dynamics

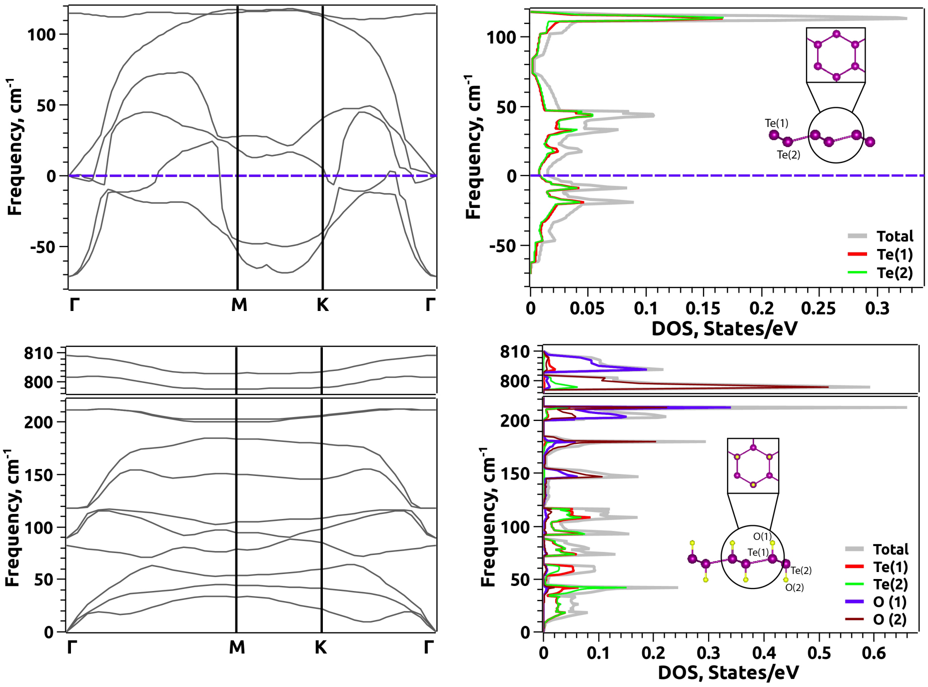

Figure 4.8: Phonon dispersion curves alongside the phonon density of states of tellurene monolayer (top) and oxygen functionalised tellurene monolayer (bottom).

We began our investigations with honeycomb lattic structures of tellurene and selenene; similar to graphene and other group IV and V elemental monolayers. Under the generalised gradient approximations, the optimized lattice constant (a) of telllurene and selenene were, 4.94 Å and 4.36 Å respectively. These structures are buckled and not planar like graphene with, buckling height (h) of 0.72 Å and 0.63 Å respectively. The angle between the tellurium atoms and selenium atoms are 114.14° and 114.29° respectively. However, we found that, the elemental monolayers i.e., tellurene and selenene are dynamically unstable since, the phonon dispersion curves indicate the presence of negative phonon frequencies (as presented in Fig. 4.8(top) and Fig. 4.10(top-left) respectively). Such dynamical unstability of tellurene and selenene is in agreement with previous studies.[49] This confirms that, electronic configurations of tellurium and selenium do not facilitate the formation of, *sp*-hybridizations and reactive surfaces due to dangling bonds.[50]

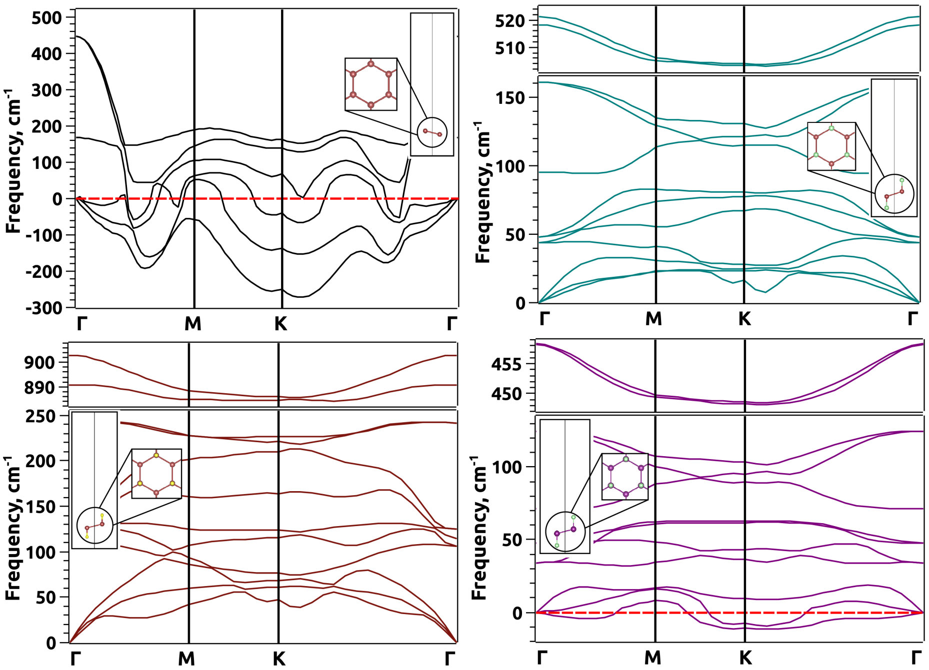

Figure 4.9: Phonon dispersion curves (inset, crystal structures) of, selenene monolayer (top-left), sulphur functionalised selenene monolayer (top-right), oxygen functionalised selenene monolayer (bottom-left) and, sulphur functionalised tellurene monolayer (bottom-right).

We proceed with functionalization of tellurene and selenene with oxygen and sulphur at alternate sub-lattice positions of the honeycomb lattice. The choice of oxygen and sulphur was made since, they can form bonds with tellurium and selenium due to their electronic configurations. The resulting structures of TeO, SeS and, SeO; did not exhibit imaginary modes or negative phonon frequencies in the entire brillouin zone (except TeS which is unstable) as evident from the phonon disperison curves presented in Fig. 4.8(bottom) and Fig. 4.9. It is worth mentioning that, the phonon dispersion curves presented in Fig. 4.9 exhibit soft phonon modes along brillouin zone path, M → K → Γ which points towards structural instability at higher temperatures. Hence, we arrive at the most sought-after honeycomb lattice structures in tellurene and selenene. These structures (presented as insets in Fig. 4.8 and 4.9) are governed by the D_{3d} point group symmetry which is lower than D_{6h} point group symmetry of graphene. This leads to a broken spatial inversion symmetry in the proposed systems. Under generalised gradient approximations, the optimized lattice constant (a) of TeO and TeS was found to be, 5.26 Å and 5.36 Å, with reduced buckling height (h) of 0.57 Å and 0.81 Å and a layer thickness (t) of 4.18 Å and 5.28 Å respectively. Similarly, the lattice constant (a);

buckling height (h) and; layer thickness (t) in SeO and SeS were found to be, 4.79 Å, 4.80 Å; 0.68 Å, 0.91 Å and 4 Å, 5.04 Å respectively. The angle between the constituent atoms in TeO; TeS; SeO and SeS were found to be, ∠O-Te-Te = 100.74°, ∠Te-Te-Te = 116.61°; ∠S-Te-Te = 104.68°, ∠Te-Te-Te = 113.80°; ∠O-Se-Se = 103.87°, ∠Se-Se-Se = 114.44° and; ∠S-Se-Se = 108.12°, ∠Se-Se-Se = 110.79° respectively. We observed that, apart from stability, the functionalization of tellurene and selenene leads to the saturation of out of plane *pz*-orbitals (also known as dangling bonds) of Te and Se; ultimately giving rise to sp^3-hybridization and enhanced spin-orbit interactions.[24,41] We discuss the qualitative and quantitative analysis of TeO and SeS in this chapter since, these systems exhibit promising and exciting properties.

Electronic Properties

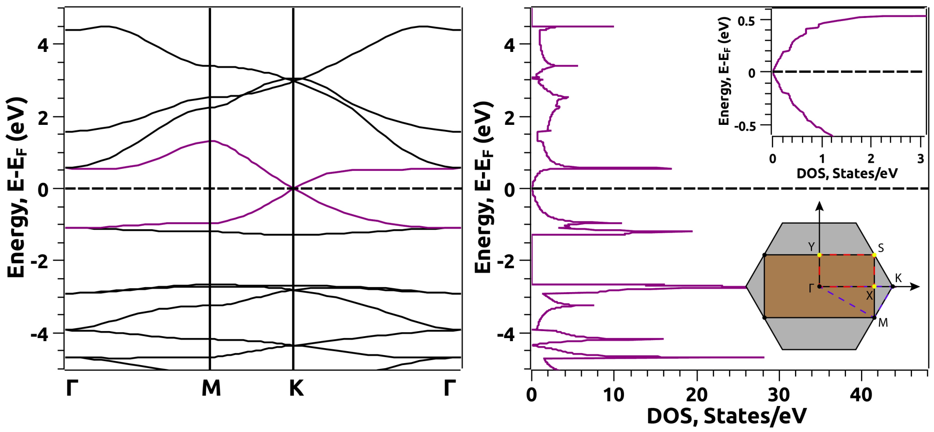

Figure 4.10: Electronic band structure and density of states indicating semi-metallic nature of TeO (inset, density of states close to Fermi level and, bulk brillouin zone with highlighted edge brillouin zone).

From Fig. 4.10 it is evident that, in the absence of spin-orbit interactions, TeO exhibits graphene-like semi-metallic with almost linear dispersions hosting Dirac degeneracies of the conduction and valence band frontiers along the high symmetry point K in the brillouin zone. Whereas, SeO and SeS exhibit a semi-conducting character with global gaps of the order of 10^{-3} eV (i.e., in SeO the gap is 1.8 meV and in SeS it is 2.3 meV as evident from Fig. 4.11) along the high symmetry point K in the brillouin zone. Since these energy gaps are far lower than the thermal energy at room temperature (which is typically 25 meV at 300 K) we can assume that, SeO and SeS would be semi-metallic in nature at room temperature.

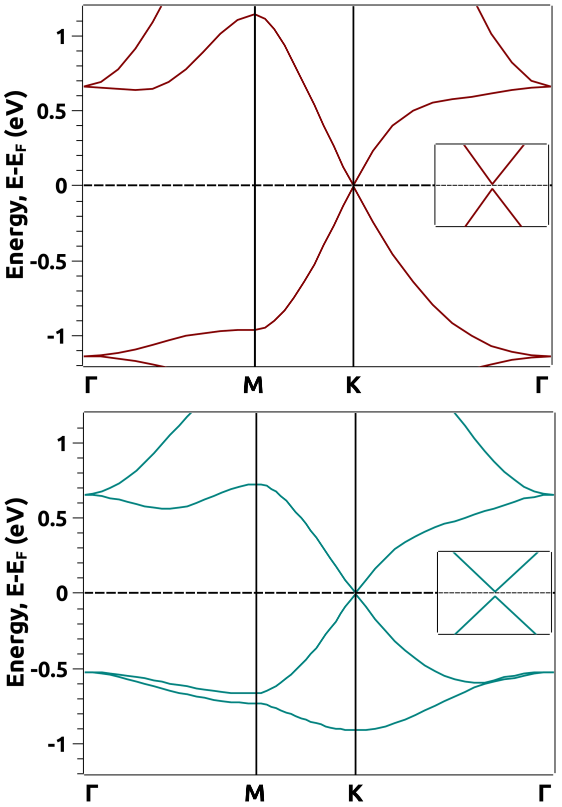

Figure 4.11: Electronic band structures of SeO (top) and SeS (bottom) in the absence of spin-orbit interactions.

The electronic band structures of TeO and SeS, with and without spin-orbit interactions are presented in Fig. 4.12. When spin-orbit interactions are considered, we observe that, the Dirac degeneracies are annihilated along the high symmetry point *K* in TeO and SeS, rendering a global large-gap of 0.365 eV and 0.167 eV respectively. Such unusual behaviour originates due to the orbital filtering effects. Since, the spin-orbit interaction induced gap is highest in TeO; we discuss it in detail in the following paragraphs (since all the effects in SeS would be similar to those as observed in TeO). The strong spin-orbit interaction can be interpreted in terms of dominant σ orbitals around the Fermi energy, rather than the π orbitals as evident Fig. 4.13(right).[35] Also, we can observe from the orbital projected density of states (presented in Fig. 4.13(left)) that the orbital inversion mechanism occurs due to the *p*-orbitals of Te and O.

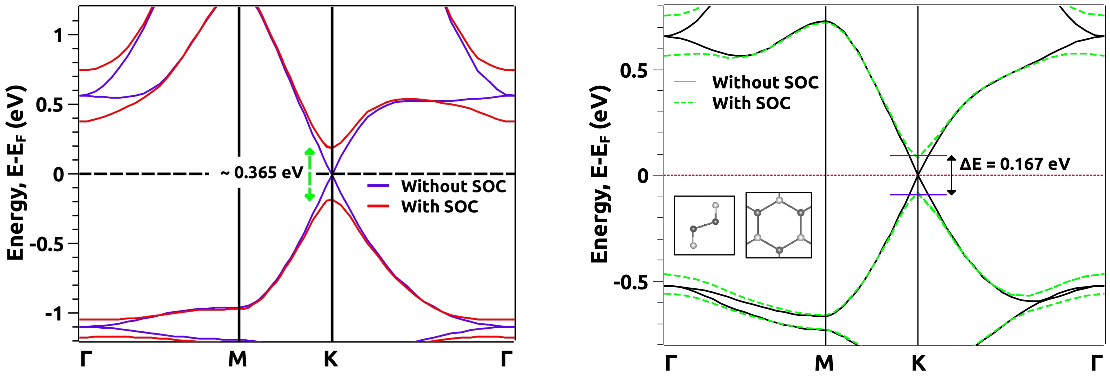

Figure 4.12: Electronic band structure of TeO (left) and SeS (right) with and without spin-orbit interactions.

Such non-trivial orbital inversions and spin-orbit interactions induced large-gap indicates towards potential non-trivial topological insulating nature of TeO. The orbital inversion mechanism is understood as; the splitting of *p*-orbital near Fermi level into; *pz* and (*px*,*py*) due to the D_{3d} point group symmetry and the D_3 groups of wave vector at Dirac degeneracies along K and K' point in the brillouin zone governing the system. Hence, the flat bands (in valence band) made up of px, py-orbitals and the massive Dirac cones make TeO unique as compared to graphene. This implies that TeO can be thought of as an orbital analog of quantum anomalous Hall effect and Wigner crystallization.[30]

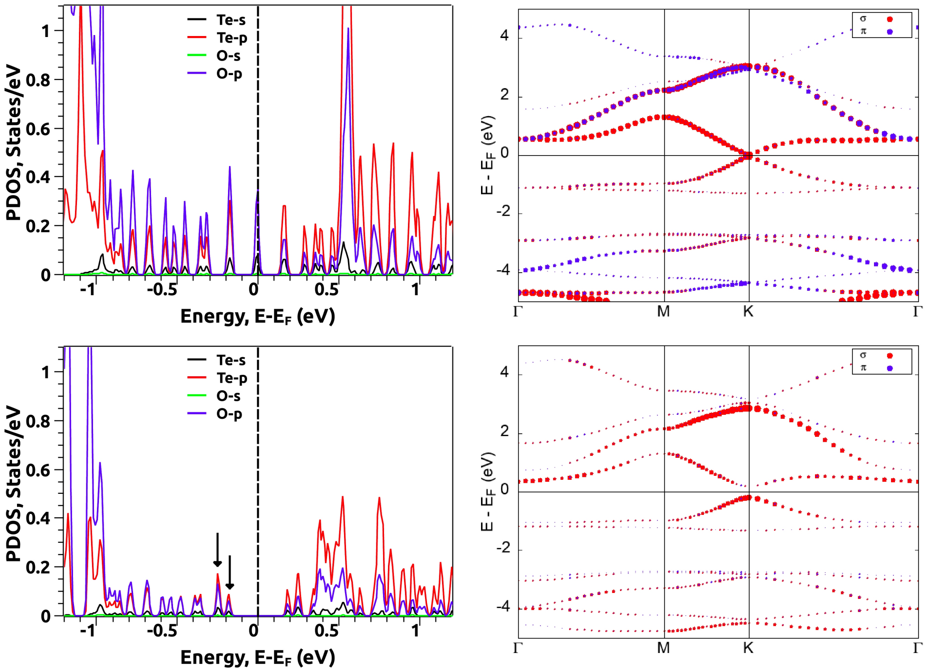

Figure 4.13: (left) Orbital projected density of states TeO (top) without and (bottom) with spin-orbit interactions indicating exchange of p-orbitals across the Fermi level highlighted by downward arrows. (right) π and σ orbitals projected electronic band structures (top) without and (bottom) with spin-orbit interactions.

Substrate Effects

Apart from the free standing monolayer of TeO discussed in previous sections, it was necessary to explore the quantum well heterostructures for practical applications. We designed van der Waals quantum well heterostructure using a 2×2 hexagonal-Boron Nitride (hBN) monolayer (as presented in Fig. 4.15). We sandwich the TeO monolayer between two layers of hBN creating a

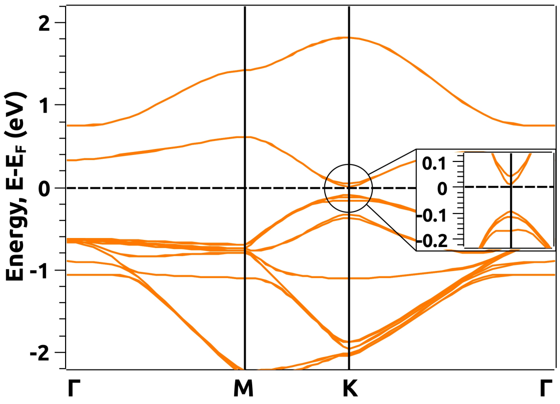

Figure 4.14: Electronic band structure of quantum well hBN/TeO/hBN.

quantum well of the form *h*BN/TeO/*h*BN. With the lattice mismatch of $\sim 4.79\%$, the interlayer separations were varied from 3 Å to 6 Å to observe the effects of van der Waals interactions at different separations. On optimizing the system by including the van der Waals correlation corrections, we observed that, TeO and *h*BN monolayers retained their original structures. On subjecting this heterostructure to a tensile strain of $\sim 14\%$ the system retained its non-trivial global gap of ~ 0.11 eV (evident from Fig. 4.14). This is considerably higher as compared to the thermal energy at room temperature with majority contribution arising from TeO around the Fermi energy.

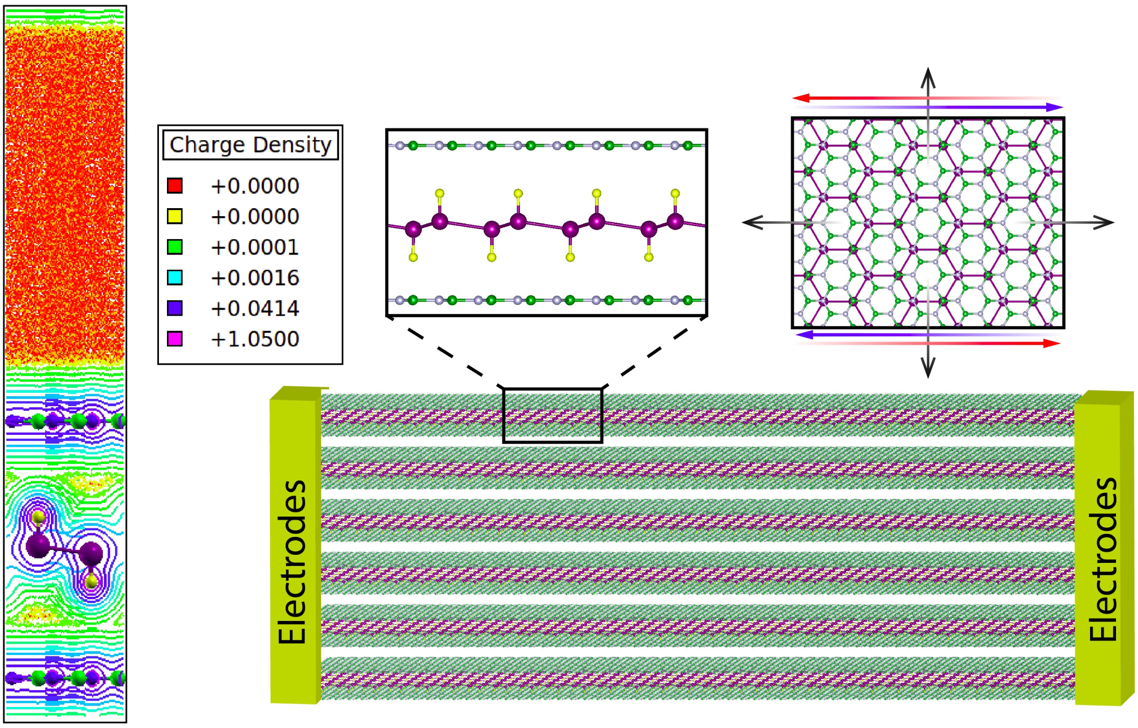

Figure 4.15: Schematic representation of van der Waals; *h*BN/TeO/*h*BN quantum well device under isotropic tensile strain.

This is due to weak interlayer coupling or absence of interlayer hybridization (as evident from the charge density plot in Fig. 4.15) of Teo and *h*BN at interlayer separation of 6 Å. Hence, the proposed structure would electrically insulate the layers of TeO protecting the spin-polarised helical edge states. This increases the number of edge transport channels to host dissipationless charge-spin transport.[37] We discuss the stability of such a heterostructure in terms of the formation / binding energy (E_b) which is defined as; $E_b = E_{hetero} - E_{TeO} - 2 \cdot E_{hBN}$, where, E_{hetero} is total energy of the heterostructure, E_{TeO} and E_{hBN} are the total energies of TeO and *h*BN monolayers. The binding energy was found to be -0.904 eV indicating that, the proposed structure under 14% tensile strain would be thermodynamically stable and experimentally viable.

Topological Properties

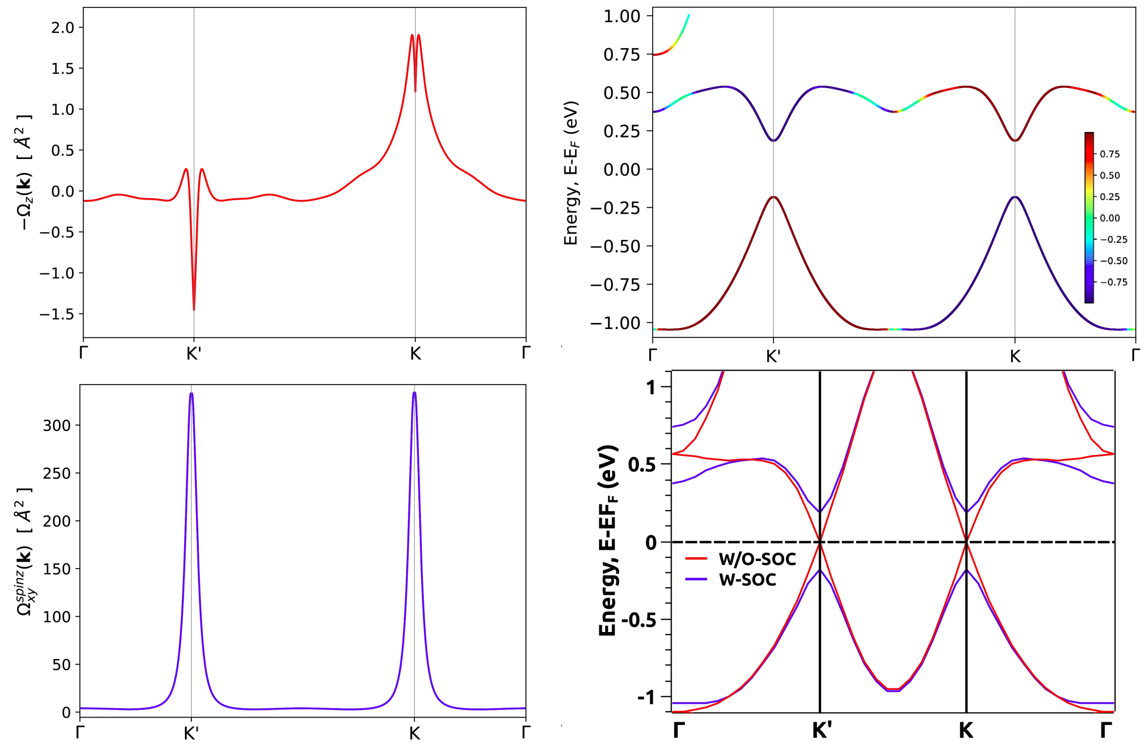

Figure 4.16: (left-top) *Berry* curvature mapping the entire brillouin zone; indicates oppposite signs. (left-bottom) k-resolved spin *Berry* curvature mapped along the brillouin zone valley points K' (area under curve = 41.57 arb. units) and K (area under curve = 41.46 arb. units). (right-top) Spin projected electronic band structure along the brillouin zone valley points K' and K (inset temperature scale indicates, positive and negative spin). (right-bottom) Electronic band structure (with and without spin-orbit interactions) along the brillouin zone valley points K' and K.

We quantified the non-trivial topological properties of TeO in terms of the $\mathbb{Z}_2$ invariant ν by using the wilson loops method around wannier charge centers. We found that, the invariant $\nu = 1$ indicates that the system is a two dimensional topological insulator. We also analysed the *Berry* curvature distribution in the entire brillouin zone (as presented in Fig. 4.16) for the nth occupied band. By integrating the *Berry* curvature throughout the brillouin zone, we found the Chern number to be $C = 1$ which further confirms the non-trivial topological insulating character of the system.

The bulk-boundary correspondance is a characteristic phenomena observed in non-trivial topological insulators. This implies that, the bulk global gap due to spin-orbit interactions would host conducting states along the edges of TeO monolayer. The edge conducting edge states are confirmed by computing the angle resolved photoemission spectroscopy-like spectra along the high symmetry paths corresponding to the orthorhombic edge brillouin zone. It is evident from Fig. 4.17 that, TeO monolayer is a two dimensional topological insulator hosting robust conducting edge states along the high symmetry point *S* of the edge brillouin zone.

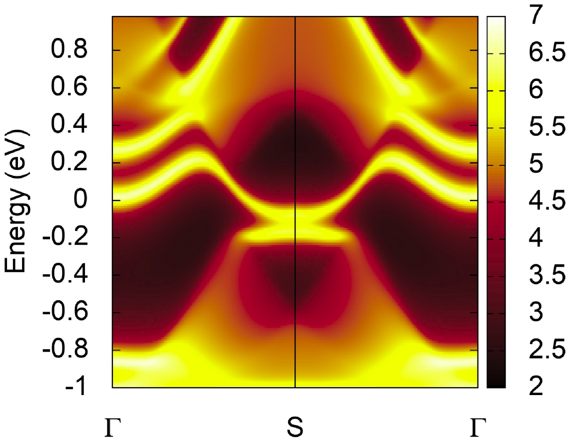

Figure 4.17: Conducting edge states in TeO.

We further analysed the origin and nature of spin Hall conductivity in TeO monolayer. As the strong spin-orbit interactions annihilate the Dirac degeneracy along the high symmetry point K in the brillouin zone (with the Fermi energy within the global gap), we can expect significantly large spin Hall conductivity.[51] This is due to the spin *Berry* curvature contributions arising from the positive and negative spins around Fermi energy which do not cancel-out excluding one sign of spin *Berry* curvature to persist. Such spin *Berry* curvature governed topology in TeO gives rise to unconventionally large transverse spin Hall conductivity (σ^z_{xy}) of the order of ≈ 63.25 $(\hbar/e)\Omega^{-1}cm^{-1}$ (as evident from Fig. 4.18).

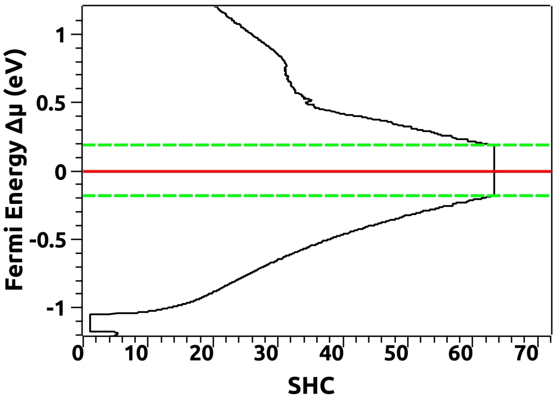

Figure 4.18: Fermi energy scan of the spin Hall conductivity ($\sigma^{spinz}_{xy}(\omega)$) in units of $(\hbar/\mathrm{e})\Omega^{-1}\mathrm{cm}^{-1}$ (red line is the Fermi level and green lines indicate non-trivial global gap).

This value is quite high as compared to other systems indicating a higher charge-spin-current conversion efficiency.[52,53] The absence of quantization in the spin Hall conductivity (as the function of Fermi energy) can be attributd to the presence of buckling in the system.[52] From the *Berry* curvature plot (presented in Fig. 4.16) we observe sharp peaks in the valley region of the brillouin zone with opposite signs at K' and K which implies that TeO can host valley Hall effects.[54] This indicates that, when the TeO monolayer is subjected to a voltage bias, the electrons from different valleys (K' and K) would experience opposite Lorentz forces which would give rise to electronic motion in opposite directions perpendicular to the drift current, eventually creating a charge-spin segregation and making the system a quantum valley Hall insulator.[55] The behaviour is clearly evident from the spin projected electronic band structure and the electronic band structures (with and without spin-orbit interactions) along the brillouin zone valley points K' and K presented in Fig. 4.16.[54]

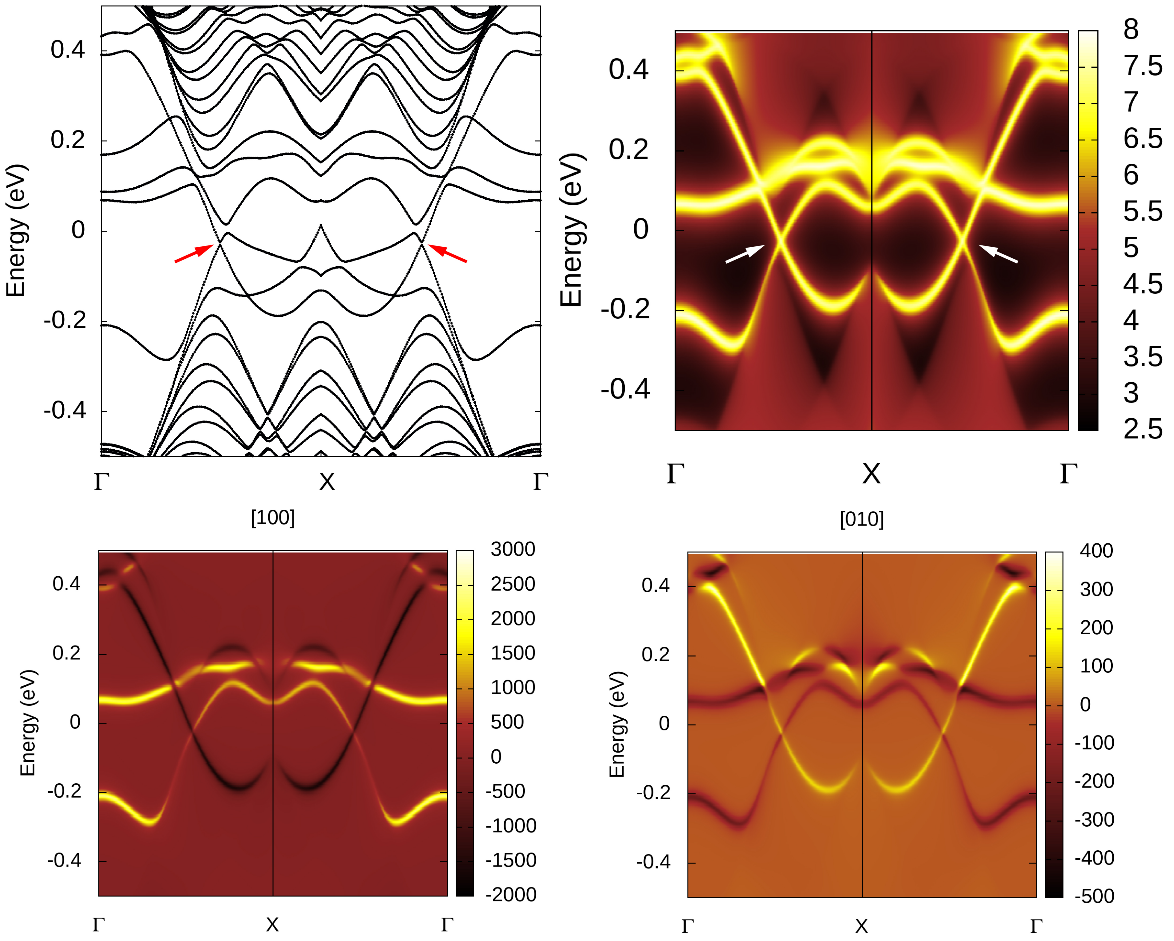

Figure 4.19: (top-left) Slab band structures indicating the conducting edge states (arrows indicate Dirac dispersions). (top-right) Angle resolved photoemission spectroscopy-like spectra indicating the conducting edge state spectra (arrows indicate Dirac dispersions). (bottom) Conducting edge spin density of states indicating spin polarizations in [100] and [010] crystal directions respectively.

Similarly, we confirmed the non-trivial topological insulating nature of SeS by plotting the slab band structures of SeS in nanoribbon configurations which are governed by the orthorhombic brillouin zone. It is evident from these slab band structures (presented in Fig. 4.19) that, SeS hosts conducting states along the edges while the bulk exhibits a global gap due to spin-orbit interactions. We also computed the angle resolved photoemission spectroscopy-like spectra which indicates conducting Dirac dispersions between the high symmetry points

Γ and X (which is equivalent to high symmetry point K in a hexagonal brillouin zone). The helical edge states of a two dimensional topological insulator are spin-polarised. This is evident from the spin-density of states along the edge crystal directions [100] and [010] which clearly indicate spin polarization as presented in Fig. 4.19. Apart from these plots, we also computed the $\mathbb{Z}_2$ invariant ν which turns out to be $\nu = 1$, confirming the non-trivial topological insulating nature of SeS monolayer.

4.3 Strain Induced Topological Insulator: AuI

By our investigations on, LiMgAs (which addressed the issue of realising a non-trivial topological behaviour in a dimensionally engineered material) and design of large-gap topological insulators TeO and SeS (wherein the partial functionalizations with oxygen and sulphur gave rise to non-trivial topological behaviour due to the orbital filtering effects) we demonstrated different methods by which non-trivial topologies can be realised in low dimensional materials. Thus contributing to the material repository which hosts previously explored two dimensional topological insulators such as in, Xenes, functionalised MXenes, transition-metal dichalcogenides and metal halides.[12,22–28,30,31,37,56–61] With our work on LiMgAs we reiterate that, if a low dimensional material does not exhibit topological insulating nature intrinsically (as observed in TeO and SeS) then, they can be explored by driving the system through a topological quantum phase transition by imposing strain on the system. In such process of materials design, we come across dilemma when, a low dimensional material hosts non-trivial topological properties but is impractical due to its toxicity. For example, Lead (Pb) based two dimensional materials are known to exhibit topological insulating properties, however, these materials are practically not viable due to the toxicity associated with Pb (with synthesis, use and recycle of such materials being next to impossible).[24] Hence, it is clear that, the process of design and prediction of a novel two dimensional topological insulator is quite challenging from materials science point-of-view. One thing that motivates the research in materials science and condensed matter physics is the versatility of a material i.e., a single material with multi-functional applications. For example, a material which is topologically insulating may be a good catalyst, may host high thermoelectric conversion efficiencies etc. With this background, we were motivated us to ask a question, can we design/realise a two dimensional topological insulator using a transition-metal element?

We therefore, explored Gold Iodide (AuI) monolayer which was dimensionally engineered from its bulk zincblende parent discussed in chapter 3. Such a system can be synthesized through conventional routes such as, chemical vapour deposition, molecular beam epitaxy and cleaving/exfoliating it from its bulk parent. Also, since AuI contains Au (which is one of the precious metals) we can explore it for multifunctional properties such as electro-catalysis, thermoelectric etc.

Structure, Lattice Dynamics and AIMD

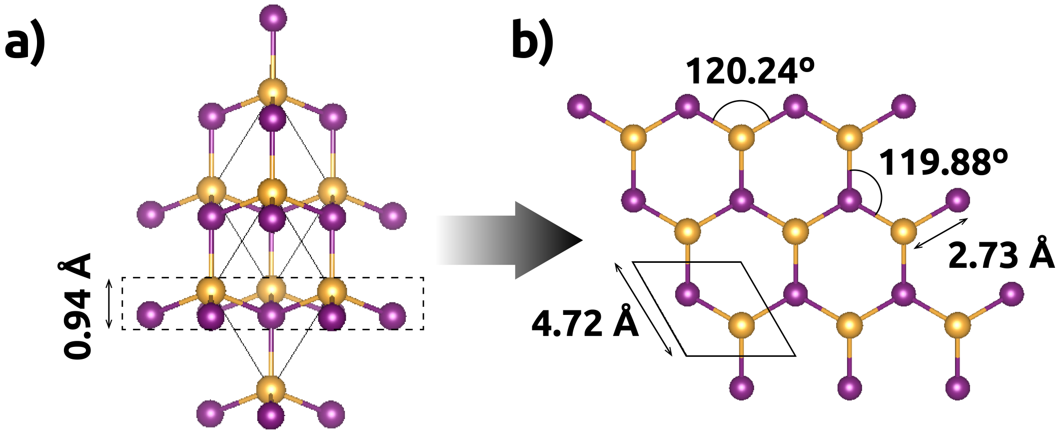

Figure 4.20: (a) Primitive cell side view of zincblende AuI with highlighted [111] crystal plane; having layer thickness of 0.94 Å. (b) Top view of [111] crystal plane isolated from the primitive cell of the zincblende AuI.

We began our investigation by isolating AuI monolayers from [111] crystal plane of the zincblende AuI structure (which exhibits topological conducting and insulating nature as discussed in chapter 3) as presented in Fig. 4.20. This structure exhibits buckling and is governed by P3m1[156] space group. However, the buckling (~ 0.94 Å) vanishes on relaxing the structure which implies that, the system undergoes a structural phase transition (as presented in Fig. 4.22). The structural phase transition occurs from the buckled phase of P3m1[156] to planar phase of P6_3mmc[194] space group. The planar structure marks the global minima under generalised gradient approximation with optimized lattice contsant (a) of 4.72 Å (with two sub-lattice positions occupied by Au and I). To simulate an ideal two dimensional monolayer, the system was confined along [001] crystal direction by introducing a vacuum of 25 Å. The bond length between Au and I is 2.73 Å, the angle ∠Au-I-Au is 119.88° and ∠I-Au-I is 120.24°.

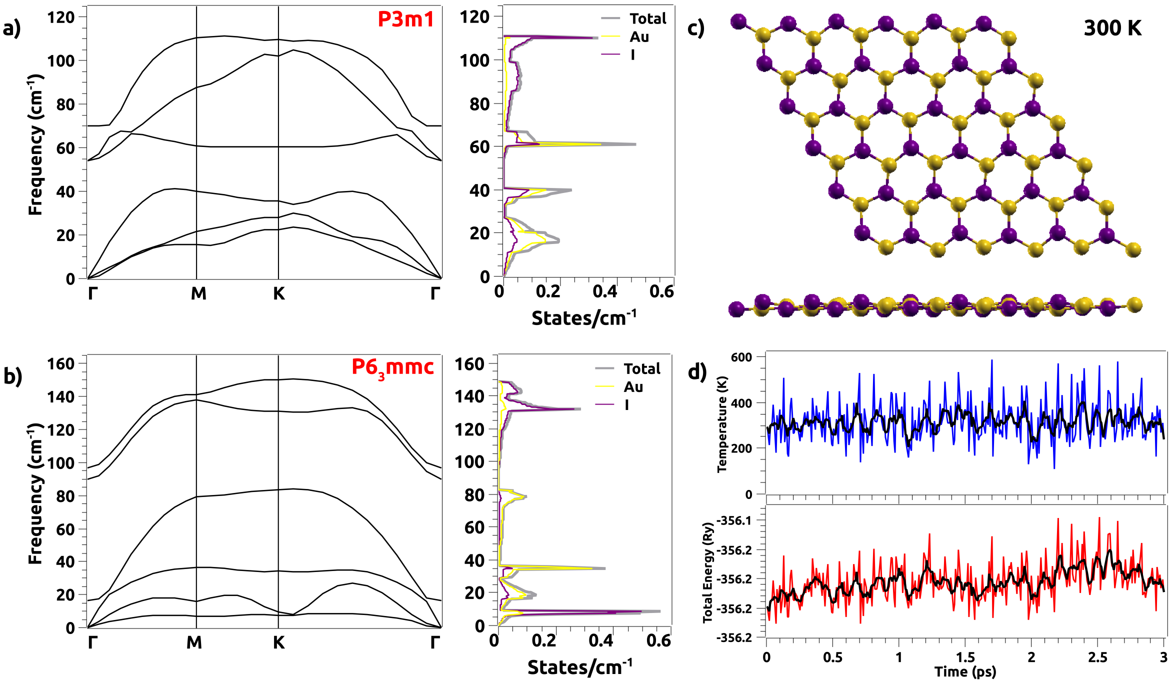

Figure 4.21: Phonon dispersion curve alongside phonon density of states indicating dynamic stability of the, (a) P3m1 phase (before relaxing the structure) and (b) P6$_3$mmc phase (after relaxing the structure) of AuI monolayer. (c) Structural stability at 300 K and 3 picoseconds time step of ab-initio molecular dynamics simulation. (d) Variation of temperature and total energy of AuI monolayer at different time steps of simulation.

Both the phases of AuI are dynamically stable as evident from the phonon dispersion curves and the phonon density of states presented in Fig. 4.21. Since there are two atoms in the unit cell, the phonon dispersion curves comprise of six phonon branches which can be decomposed into three acoustic and three optical branches. It is evident from the phonon dispersion curves that, the longitudinal and transverse optical (LO-TO) modes are non-degenerate at the center of the brillouin zone indicating towards the ionic character of AuI which is governed by long-range Coulomb interactions. Also, the out-of-plane ZA and ZO modes in the acoustic and optical branches confirm the two dimensional nature of the system. We also compute the formation energy (given by, $E_f = E_{AuI} - E_{Au} - E_I$ where, E$_X$ (X = AuI, Au, I) are the total energies) to get insights into the thermodynamic stability and viability of the proposed system. We found that, the ground state of AuI monolayer turns out to be highly thermodynamically stable with formation energy of the order of −3.814 eV/atom which is lower than the formation energy of the zincblende parent i.e., −3.551 eV/atom. This implies that, AuI monolayers can be synthesized via conventional methods such as, chemical vapour deposition or molecular beam epitaxy ensuring layer-by-layer growth of a material along the crystal direction of choice. Also, from the ab-initio molecular dynamics simulations at 300 K we found that, the structural intigrity is retained throughout the 3 picoseconds (3000 femtoseconds) simulation time indicating that, AuI monolayer would be stable at room temperature.

Electronic Properties

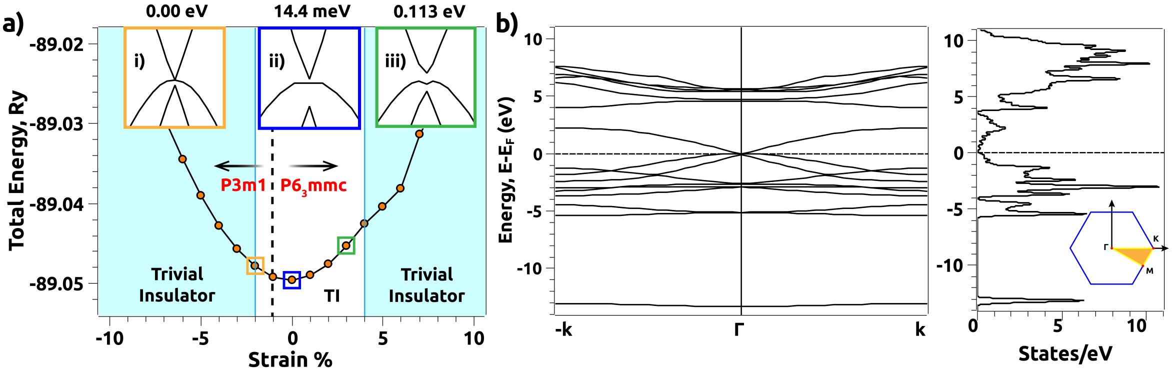

Figure 4.22: (a) Total energy (in Ry units) variation with % strain. The cyan background indicate trivial insulator nature of AuI and white region indicates topological insulating nature. The black dashed line marks the structural phase transition from P3m1 to P6$_3$mmc phase. (i) Critical DP at 2% strain, ii) narrow gap at 0% strain and, iii) enhanced gap at 3% strain. (b) Electronic band structure at 0% strain alongside density of states with inset of hexagonal brillouin zone.

Under pristine conditions (i.e., in the ground state at 0% strain) the planar phase of AuI exhibits a narrow gap of $\sim$ 14.4 meV (as evident from Fig. 4.22(a(ii))) at the brillouin zone center (as presented in Fig. 4.22(b)). This phase marks the global minima of as evident from the energy versus strain plot in Fig. 4.22(a). Now, to realise a non-trivial topological quantum phase transition and to investigate the topological character of the gap at 0% strain, we search for a critical Dirac point in the vicinity of global minima by imposing bi-axial compressive and tensile strain of $\pm$10%. We found that, the critical point hosting Dirac degeneracy exists at a compressive strain of -2% (as resented in Fig. 4.22(a(i))). Hence, -2% marks the lower boundary of the non-trivial topological quantum phase transitions. Below this strain, the system exhibits trivial semi-conducting nature hosting a global band gap of 0.5 eV at -5% strain and 0.8 eV at -10% strain along the brillouin zone center. We performed qualitative analysis of the non-trivial topological quantum phase transition in terms of the orbital projected density of states presented in Fig. 4.23. It is evident from the orbital projected density of states that, at -2% strain (i.e., critical point) and the strain regime below it; the valence band is populated with *p-d* hybrid orbitals of I and Au respectively (as evident from Fig. 4.23(a)) and the conduction band is populated by the s-orbitals of Au and I and *s-p* hybrid orbitals of Au and I (as evident from Fig. 4.23(a)). Such orbital distributions are common in transition metal based topological insulators or topological materials due to partially filled *d*-orbitals.[36,62,63]

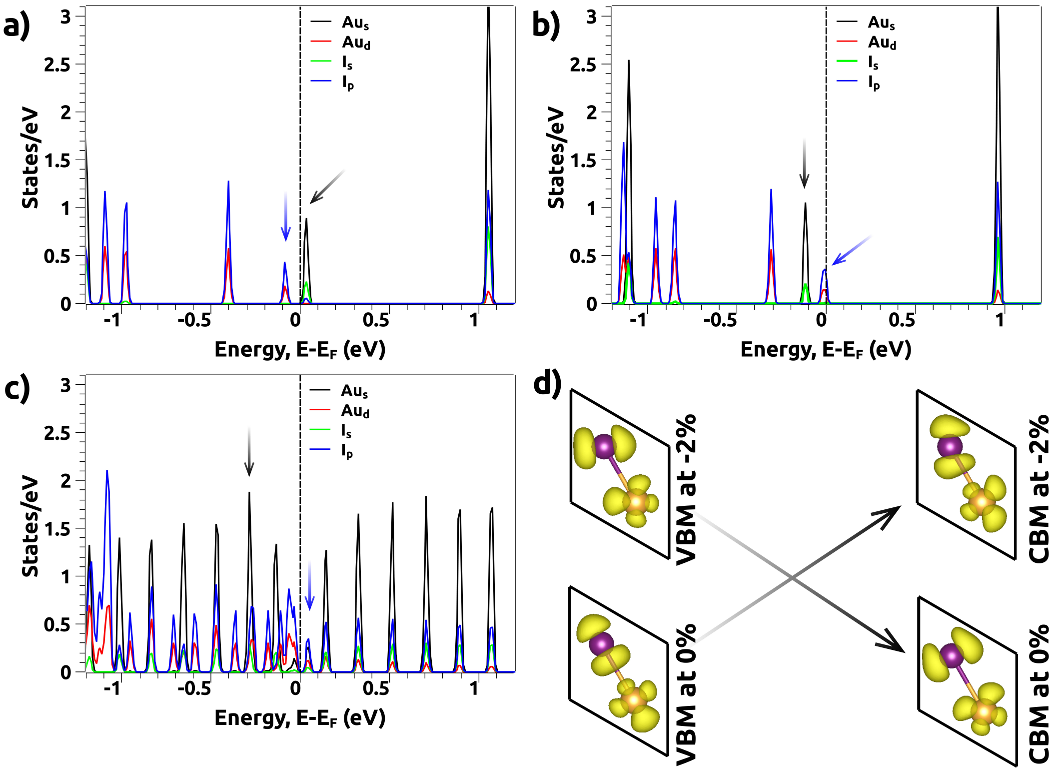

Figure 4.23: Orbital projected density of states at: (a) 2% strain, (b) 0% strain, and (c) 3% strain. (d) Topological quantum phase transitions in terms of the inversion of the electron localization functions.

On increasing the strain from the critical point (at −2%) towards the positive regime (i.e., towards the upper boundary) we observed that the band gap increases from ∼ 14.4 meV (at 0% strain) to 0.113 eV (at 3% strain) with orbital and band dispersion inversions becoming prominent (as evident from Fig. 4.23(b-c) and Fig. 4.22(a(ii-iii))). It is clear from the orbital projected density of states that, the *s*-orbitals of Au and I cross the Fermi level (at 0% strain, Fig. 4.23(b)) and completely populate the valence band at 3% strain by explicit exchange of the p-d hybrid orbitals and *s*-orbitals of Au and I across the Fermi level (as evident in Fig. 4.23(c)) leading to a large non-trivial gap at 3% strain. The non-trivial nature is further confirmed by computing the electron localization functions at −2% (critical strain) and 0% strain (as presented in Fig. 4.23(d)). It is evident that, the features of the electron localization functions are exchanged indicating a topological quantum phase transition. The non-trivial nature can be attributed to the strong spin-orbit interactions between the core and valence *d*-orbital electrons of Au.[62] It was observed that, the narrow gap at 0% strain gets enhanced by the virtue of strain as evident from the band dispersions presented in Fig.

4.22(a(ii-iii)). This global spin-orbit interaction induced gap is superior as compared to other well known two dimensional topological insulators such as, graphene, selenene, germanene etc.[12,22–24,27,31] The non-trivial topological quantum phase transitions are accompanied by anamolous structural phase transitions. Usually, the buckling height should increase under compressive strain and decreases under tensile strain however, in AuI monolayer, we observe an inversion in the atomic positions along z-direction (i.e., under compressive strain sub-lattice Au is at top and sub-lattice I is at bottom whereas, under tensile strain this gets inverted; causing an inverted buckling with the monolayer eventually becoming planar). Such anamolous nature leads to orbital alterations giving rise to extra degrees of freedom for electrons and imposes a lorentz force on electrons causing to spin-charge accumulation along the edges.

Topological Properties

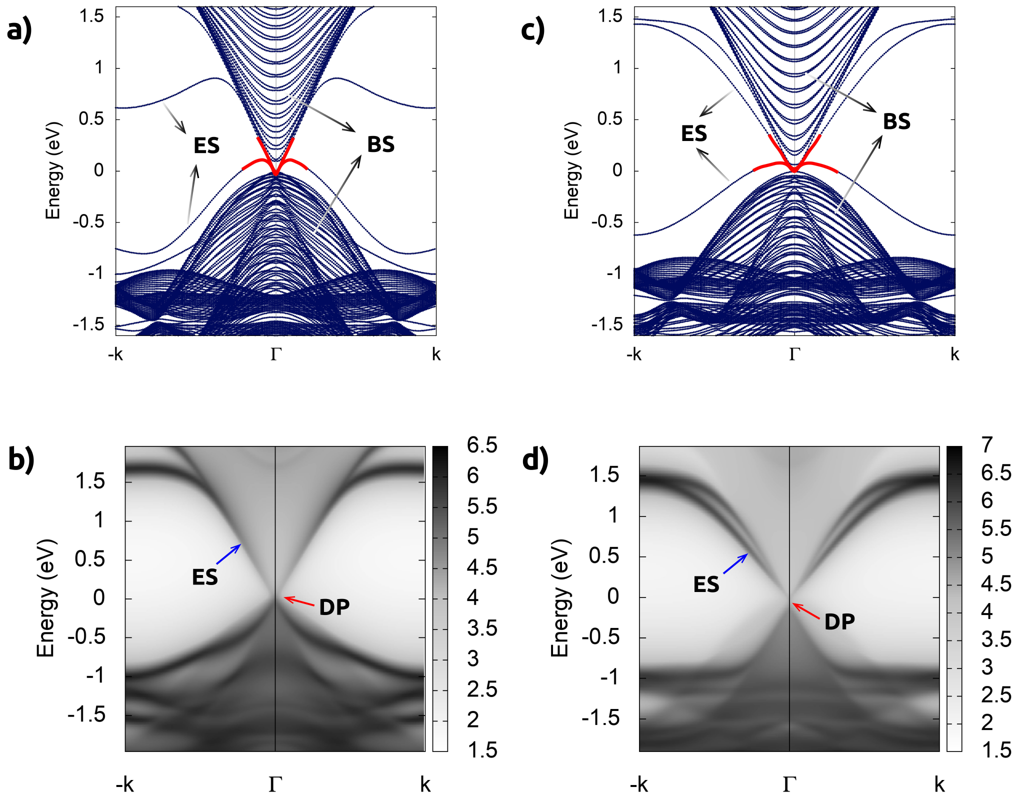

Figure 4.24: (a,b) Slab band structure and edge state spectra at 0% strain indicating the bulk states, edge states and, the Dirac point. (c,d) Slab band structure and edge state spectra at 3% strain indicating the bulk states, edge states and, the Dirac point.

To confirm the non-trivial nature, we computed the $\mathbb{Z}_2$ invariant ν, slab band structures and angle resolved photoemission spectroscopy-like spectra. Using the wilson loop method around wannier charge centers we found that, AuI monolayer is indeed a non-trivial two dimensional topological insulator with $\mathbb{Z}_2$ invariant $\nu = 1$ in the range of strain from -1% to 3%. Since the non-trivial spin-orbit interactions induced gap at 0% strain was enhance by strain engineering to a large-gap at 3% strain, we had to verify the persistance of conducting edge states. For this purpose we computed angle resolved photoemission spectroscopy-like spectra at 0% strain and 3% strain (as presented in Fig. 4.24). It is evident from the slab band structures (for nanoribbon configuration of AuI) in Fig. 4.24(a,c) that, AuI monolayer at 0% and 3% strain hosts conducting edge states with Dirac points at the center of the brillouin zone. These states would be robust against deformations and non-magnetic impurities. Similarly, from Fig. 4.24(b,d) it is clear that, the Dirac dispersion along the edges of AuI monolayer would persist at 0% as well as 3% strain.

4.4 Conclusion

We presented our investigations on the dimensional engineering of non-trivial two dimensional topological insulator LiMgAs from trivial bulk parent. As expected, this system presented non-trivial topological quantum phase transitions at low pressure due to quantum confinement effects and large surface-volume ratio. The proposed monolayer of LiMgAs was found to be dynamically stable with absence of negative phonon frequencies in the entire brillouin zone. Also, the non-trivial phase of LiMgAs monolayer exhibits unconventional Fermion velocities along different directions of the brillouin zone. The non-trivial topological phase transition in this system is characterised by *s*-*p* orbital inversions across the Fermi level accompanying the inversion in band dispersions. This system is proposed to exhibit room temperature applications owing to large-gap induced by spin-orbit interactions. Also, we compared the band inversion strength which is stronger as compared to the bulk parent, indicating towards the underlying quantum confinement effects. We finally confirmed the non-trivial nature by computing the $\mathbb{Z}_2$ invariant which was $\nu = 1$ and edge state spectra indicating a conducting Dirac dispersion along the edge brillouin zone path.

To further increase the non-trivial gap solely due to spin-orbit interactions i.e., without applying strain, we explored functionalization technique. We presented, elemental monolayers of Tellurium and Selenium for the first time. According to previous reports in literature, we too observed that, the free-standing elemental monolayers are dynamically unstable. However, on partially functionalizing these monolayers with oxygen and sulphur (since, they would form bonds due to mutually favourable electronic configurations) we observed that TeO, SeS and SeS were dynamically stable except TeS. These stable monolayers were then explored for their electronic properties and we found that both, TeO and SeS present are large-gap systems under the influence of spin-orbit interactions. On inclusion of spin-orbit interactions we observed *s*-*p* orbital inversions across the Fermi indicating towards potential non-trivial character of TeO and SeS. The effect was attributed to orbital filtering effects which saturate the dangle bonds (originating from the pz-orbitals) in z-direction giving rise to extra degrees of freedom to the electrons. This was confirmed by plotting the π and σ orbital projected band structures. We performed in depth analysis of TeO since it exhibited highest non-trivial gap under spin-orbit interactions of 0.365 eV. We presented the Berry curvature and spin-Berry curvature analysis of TeO in the non-trivial regime under the influence of spin-orbit interactions. From the analysis we observed that, TeO can be used for spintronic and valleytronic applications, due to the opposite Lorentz forces acting on the electrons which leads to the spin-charge accumulation along the edges. This was presented in terms of the spin-projected electronic band structure along the two valleys points in the brillouin zone. The large-gap induced due to spin-orbit interactions also leads to unconventionally high spin Hall conductivity in the global gap (which was observed to be superior to several other materials). From experimental perspective, we also presented the investigations of quantum well *h*BN/TeO/*h*BN which was found to retain the large-gap due to spin-orbit interactions under a tensile strain of 14%. These computations were followed by computing the edge state spectra of TeO and SeS. Clearly, TeO and SeS presented Dirac dispersions along the edge brillouin zone path. Also, we presented that the spin channels along the edges of SeS traverse in opposite directions by plotting the edge spectra along the [100] and [010] crystal directions. Ultimately, we presented the $\mathbb{Z}_2$ invariant which was found to be $\nu = 1$ indicating that, the non-trivial characters are indeed topological in nature and that, TeO and SeS are two dimensional topological insulators.

Similar to the dimensional engineering of LiMgAs from bulk parent, we presented the dimensionally engineered AuI monolayer. We saw that, due to quantum confinement effects, the low dimensional phase exhibits a narrow gap as compared to the bulk parent which exhibits semi-metallic character. The ground state of this system was found to exhibit buckled structure governed by the P3m1 space group rather than P6_3mmc space group. However, in the P3m1 phase, AuI monolayer presented a gap of 14.4 meV, from here we subjected the system to compressive and tensile pressures to mark the topological quantum phase transition boundaries. We found that, the lower boundary was at -2% and the upper boundary was at 4%, within this region, AuI presented non-trivial topological insulating phase in two different structural phases of P3m1 and P6_3mmc with the non-trivial gap as high as 0.113 eV under spin-orbit interactions. The underlying mechanism was found to be unconventional *s*, *p*-*d* orbital inversion mechanism alongwith the inverted band disperions. Also, we presented the inversion mechanism in terms of the exchange of charge densities or electron localisation functions across the Fermi level. To ascertain that, the non-trivial nature persists at the pressure of 3% (where the spin-orbit interactions induced gap is 0.113 eV) we computed the slab band structures and the edge state spectra both of which clearly host the non-trivial Dirac like edge dispersion in the edge brillouin zone. Finally we present the $\mathbb{Z}_2$ invariant and find that it is $\nu = 1$ in the region of -2% to 4% strain.

* * *

Bibliography

[1] Charles L Kane and Eugene J Mele.Physical review letters, 95(14):146802, 2005.

[2] Charles L Kane and Eugene J Mele.Physical review letters, 95(22):226801, 2005.

[3] B Andrei Bernevig and Shou-Cheng Zhang.Physical review letters, 96(10):106802, 2006.

[4] M Zahid Hasan and Charles L Kane.Reviews of modern physics, 82(4):3045, 2010.

[5] Changhyun Han, Minsu Kang, and Heonsu Jeon.ACS Photonics, 7(8):2027–2036, 2020.

[6] AH Castro Neto, Francisco Guinea, Nuno MR Peres, Kostya S Novoselov, and Andre K Geim.Reviews of modern physics, 81(1):109, 2009.

[7] Lukas Muchler, Frederick Casper, Binghai Yan, Stanislav Chadov, and Claudia Felser, physica status solidi (RRL)–Rapid Research Letters, 7(1-2), 91-100, 2013.

[8] Motohiko Ezawa.New Journal of Physics, 14(3):033003, 2012.

[9] Motohiko Ezawa.Journal of the Physical Society of Japan, 84(12):121003, 2015.

[10] Ranber Singh.International Journal of Modern Physics B, 32(05):1850055, 2018.

[11] Gul Rahman, Asad Mahmood, and Victor M. Garcia-Suarez.Scientific Reports, 9(1):7966, May 2019.

[12] Mingwen Zhao, Xiaoming Zhang, and Linyang Li.Scientific Reports, 5(1):16108, Nov 2015.

[13] Shashwat Anand, Krishnamohan Thekkepat, and Umesh V. Waghmare.Nano Letters, 16(1):126–131, Jan 2016.

[14] Zhongfei Liu, Peihong Wang, Qiaoyu Cui, Guang Yang, Shaowei Jin, and Kuangwei Xiong.RSC Adv., 9:2740–2745, 2019.

[15] Arun Bansil, Hsin Lin, and Tanmoy Das.Reviews of Modern Physics, 88(2):021004, 2016.

[16] Kulwinder Kaur, Shobhna Dhiman, and Ranjan Kumar.Physics Letters A, 381(4):339–343, 2017.

[17] Cheng-Cheng Liu, Hua Jiang, and Yugui Yao.Phys. Rev. B, 84:195430, Nov 2011.

[18] Joel E. Moore.Nature, 464(7286):194–198, Mar 2010.

[19] Edirisuriya M. D. Siriwardane and Deniz Çakir.Journal of Applied Physics, 125(8):082527, 2019.

[20] Yugui Yao, Fei Ye, Xiao-Liang Qi, Shou-Cheng Zhang, and Zhong Fang.Physical Review B, 75(4):041401, 2007.

[21] Sergej Konschuh, Martin Gmitra, and Jaroslav Fabian.Physical Review B, 82(24):245412, 2010.

[22] Jialiang Deng, Bingyu Xia, Xiaochuan Ma, Haoqi Chen, Huan Shan, Xiaofang Zhai, Bin Li, Aidi Zhao, Yong Xu, Wenhui Duan, et al.Nature materials, 17(12):1081–1086, 2018.

[23] Cheng-Cheng Liu, Wanxiang Feng, and Yugui Yao.Physical review letters, 107(7):076802, 2011.

[24] Yong Xu, Binghai Yan, Hai-Jun Zhang, Jing Wang, Gang Xu, Peizhe Tang, Wenhui Duan, and Shou-Cheng Zhang.Physical review letters, 111(13):136804, 2013.

[25] Qihang Liu, Xiuwen Zhang, LB Abdalla, Adalberto Fazzio, and Alex Zunger.Nano letters, 15(2):1222–1228, 2015.

[26] Guang Yang, Ze Xu, Zhongfei Liu, Shaowei Jin, Haijun Zhang, and Zongling Ding, The Journal of Physical Chemistry C, 121(23):12945–12952, 2017.

[27] Ya-ping Wang, Chang-wen Zhang, Wei-xiao Ji, Run-wu Zhang, Ping Li, Pei-ji Wang, Miao-juan Ren, Xin-lian Chen, and Min Yuan.Journal of Physics D: Applied Physics, 49(5):055305, 2016.

[28] Ya-ping Wang, Wei-xiao Ji, Chang-wen Zhang, Ping Li, Feng Li, Miao-juan Ren, Xin-Lian Chen, Min Yuan, and Pei-ji Wang.Scientific reports, 6(1):1–8, 2016.

[29] Mingwen Zhao, Xiaoming Zhang, and Linyang Li.Scientific reports, 5(1):1–7, 2015.

[30] Zhigang Song, Cheng-Cheng Liu, Jinbo Yang, Jingzhi Han, Meng Ye, Botao Fu, Yingchang Yang, Qian Niu, Jing Lu, and Yugui Yao.NPG Asia Materials, 6(12):e147–e147, 2014.

[31] Lede Xian, Alejandro Perez Paz, Elisabeth Bianco, Pulickel M Ajayan, and Angel Rubio.2D Materials, 4(4):041003, 2017.

[32] Run-Wu Zhang, Chang-Wen Zhang, Wei-Xiao Ji, Shi-Shen Yan, and Yu-Gui Yao, Nanoscale, 9(24):8207–8212, 2017.

[33] Xing-Kai Hu, Ji-Kai Lyu, Chang-Wen Zhang, Pei-Ji Wang, Wei-Xiao Ji, and Ping Li, Physical Chemistry Chemical Physics, 20(19):13632–13636, 2018.

[34] Miao Zhou, Wenmei Ming, Zheng Liu, Zhengfei Wang, Ping Li, and Feng Liu, Proceedings of the National Academy of Sciences, 111(40):14378–14381, 2014.

[35] Chen Si, Junwei Liu, Yong Xu, Jian Wu, Bing-Lin Gu, and Wenhui Duan.Physical Review B, 89(11):115429, 2014.

[36] Hongming Weng, Ahmad Ranjbar, Yunye Liang, Zhida Song, Mohammad Khazaei, Seiji Yunoki, Masao Arai, Yoshiyuki Kawazoe, Zhong Fang, and Xi Dai.Physical Review B, 92(7):075436, 2015.

[37] Ya-ping Wang, Wei-xiao Ji, Chang-wen Zhang, Ping Li, Shu-feng Zhang, Pei-ji Wang, Sheng-shi Li, and Shi-shen Yan.Applied Physics Letters, 110(21):213101, 2017.

[38] Yunye Liang, Mohammad Khazaei, Ahmad Ranjbar, Masao Arai, Seiji Yunoki, Yoshiyuki Kawazoe, Hongming Weng, and Zhong Fang.Physical Review B, 96(19):195414, 2017.

[39] Lauryn Wu, Kunming Gu, and Qiliang Li.Applied Surface Science, 484:1208–1213, 2019.

[40] Xing-kai Hu, Yong Wang, and Ping Li.Chemical Physics Letters, 740:137064, 2020.

[41] Zhi-Quan Huang, Mei-Ling Xu, Gennevieve Macam, Chia-Hsiu Hsu, and Feng-Chuan Chuang.Physical Review B, 102(7):075306, 2020.

[42] Ming-Yang Liu, Long Gong, Wen-Zhong Li, Meng-Long Zhang, Yao He, and Chao Cao.Applied Surface Science, 540:148268, 2021.

[43] Chen Si, Kyung-Hwan Jin, Jian Zhou, Zhimei Sun, and Feng Liu.Nano letters, 16(10):6584–6591, 2016.

[44] Lin Miao, Meng-Yu Yao, Wenmei Ming, Fengfeng Zhu, CQ Han, ZF Wang, DD Guan, CL Gao, Canhua Liu, Feng Liu, et al.Physical Review B, 91(20):205414, 2015.

[45] Huang, Xiaochun and Guan, Jiaqi and Lin, Zijian and Liu, Bing and Xing, Shuya and Wang, Weihua and Guo, Jiandong, Nano letters, 17(8), 4619–4623, 2017.

[46] Zhu, Zhili and Cai, Xiaolin and Yi, Seho and Chen, Jinglei and Dai, Yawei and Niu, Chunyao and Guo, Zhengxiao and Xie, Maohai and Liu, Feng and Cho, Jun-Hyung and others, Physical review letters, 119(10), 106101, 2017.

[47] Jingkai Qin, Gang Qiu, Jie Jian, Hong Zhou, Lingming Yang, Adam Charnas, Dmitry Y Zemlyanov, Cheng-Yan Xu, Xianfan Xu, Wenzhuo Wu, et al.ACS nano, 11(10):10222–10229, 2017.

[48] Meryem Bouaziz, Wei Zhang, Yongfeng Tong, Hamid Oughaddou, Hanna Enriquez, Rym Mlika, Hafsa Korri-Youssoufi, Zhesheng Chen, Heqi Xiong, Yingchun Cheng, et al.2D Materials, 8(1):015029, 2020.

[49] Aidi Zhao and Bing Wang.APL Materials, 8(3):030701, 2020.

[50] Dongchao Wang, Li Chen, Changmin Shi, Xiaoli Wang, Guangliang Cui, Pinhua Zhang, and Yeqing Chen.Scientific reports, 6(1):1–7, 2016.

[51] Xuelei Sui, Chong Wang, Jinwoong Kim, Jianfeng Wang, SH Rhim, Wenhui Duan, and Nicholas Kioussis.Physical Review B, 96(24):241105, 2017.

[52] S. M. Farzaneh and Shaloo Rakheja.Phys. Rev. B, 104:115205, Sep 2021.

[53] Filipe Matusalem, Marcelo Marques, Lara K Teles, Lars Matthes, Jurgen Furthmuller, and Friedhelm Bechstedt.Physical Review B, 100(24):245430, 2019.

[54] Baozeng Zhou, Zheng Li, Jiaming Wang, Xuechen Niu, and Chongbiao Luan, Nanoscale, 11(28):13567–13575, 2019.

[55] Tong Zhou, Jiayong Zhang, Hua Jiang, Igor Zutic, and Zhongqin Yang.npj Quantum Materials, 3(1):1–7, 2018.

[56] Xiaofeng Qian, Junwei Liu, Liang Fu, and Ju Li.Science, 346(6215):1344–1347, 2014.

[57] Liujiang Zhou, Liangzhi Kou, Yan Sun, Claudia Felser, Feiming Hu, Guangcun Shan, Sean C Smith, Binghai Yan, and Thomas Frauenheim.Nano letters, 15(12):7867–7872, 2015.

[58] Alessandro Molle, Joshua Goldberger, Michel Houssa, Yong Xu, Shou-Cheng Zhang, and Deji Akinwande.Nature materials, 16(2):163–169, 2017.

[59] Sheng-shi Li, Wei-xiao Ji, Shu-jun Hu, Chang-wen Zhang, and Shi-shen Yan.ACS applied materials & interfaces, 9(47):41443–41453, 2017.

[60] Meng-Han Zhang, Shu-Feng Zhang, Pei-Ji Wang, and Chang-Wen Zhang.Nanoscale, 12(6):3950–3957, 2020.

[61] Shou-juan Zhang, Chang-wen Zhang, Shu-feng Zhang, Wei-xiao Ji, Ping Li, Pei-ji Wang, Sheng-shi Li, and Shi-shen Yan.Physical Review B, 96(20):205433, 2017.

[62] Duk-Hyun Choe, Ha-Jun Sung, and Kee Joo Chang.Physical Review B, 93(12):125109, 2016.

[63] Runhan Li, Hao Wang, Ning Mao, Hongkai Ma, Baibiao Huang, Ying Dai, and Chengwang Niu.Applied Physics Letters, 119(17):173105, 2021.

* * *